Instability of ABO_3 perovskite surfaces induced by vacancy formation (A = Ca, Sr, Ba; B = Ti, Zr, Sn)

Ned Thaddeus Taylor [1,*], Michael Thomas Morgan [1,2,3,4] and Steven Paul Hepplestone [1,†]

[1] *Department of Physics and Astronomy, University of Exeter, Stocker Road, Exeter EX4 4QL, United Kingdom*

[2] *Catalan Institute of Nanoscience and Nanotechnology (ICN2), CSIC and BIST, Campus UAB, Bellaterra, 08193 Barcelona, Spain*

[3] *Physics Department, Autonomous University of Barcelona (UAB), Campus UAB, Bellaterra, 08193 Barcelona, Spain*

[4] *Royal Melbourne Institute of Technology, School of Engineering, GPO Box 2476, Melbourne VIC 3001, Australia*

(Received 25 May 2023; revised 23 April 2025; accepted 4 June 2025; published 8 July 2025)

This work presents a first-principles study of the (001) surface energetics of nine ABO_3 perovskites (A = Ca, Sr, Ba; B = Ti, Zr, Sn), with a focus on the role of surface vacancies in determining termination stability. Additionally, investigation into the behavior of vacancies as a function of depth from the surface in these perovskites is carried out, and results are compared to formation of the vacancies in bulk. Combining results from these investigations reveals a general trend for all nine perovskites: the undefected AO surface is more energetically favorable to form than the BO_2 surface. This dominance of the AO over the BO_2 surface is further enforced by the phase diagrams of perovskite surfaces. However, A-site vacancies at the AO surface are far more favorable (1–2 eV lower in energy) than B-site vacancies at the BO_2 surface. Charged vacancies only drive this further under oxygen-rich conditions, showing a smaller range of stability for the AO than the BO_2 surface. These results indicate that, while the AO surface is easier to form, the BO_2 surface will display better long-term stability, making it more suitable for use in potential applications. This study furthers the understanding of oxide perovskite (001)-terminated surface stability, which will aid in surface growth and manufacturing.

DOI: 10.1103/w683-tvc4

I. INTRODUCTION

The basic chemical formula of oxide perovskites, ABO_3, can be easily customized by changing the cation sites (A and B), which results in materials with different properties. Because of this, the material grouping has received great attention for many years in a wide range of fields, including metal-insulator transition [1], two-dimensional electron gas formation [2–4], catalysis [5,6], photocatalysis [7], and many more [8–11]. Much of the desirability of oxide perovskites stems from application of their surfaces and interfaces, so understanding their surface properties is key to determining their potential. With different surfaces exhibiting a variety of properties, finding a way to reliably manufacture the desired surface, in addition to assessing the stability of said surface, is essential.

ABO_3 structures tend to involve covalent bonds forming between B and O atoms, which in turn form a cage around each ionically bonded A-site atom [12]. Recent attempts to manufacture (001) perovskite oxide surfaces have highlighted the difficulties involved, with multiple experimental studies producing different pristine (001) perovskite oxide surfaces [13–20]. Many attempts to form pristine surfaces have focused on using one or a combination of annealing, grinding, polishing, and cleaving. Samples terminated on the (001) plane that are produced through cleaving and postannealing contain both AO and BO_2 terminations [15], while, for ground and polished processes, the surface area is found to be dominated by BO_2 termination (75%–95% for $SrTiO_3$ single-crystalline substrates) [16]. Further investigations have shown that, while BO_2 surfaces are more dominant for short surface treatment timescales and low temperatures, the AO surface becomes dominant the longer it is treated and higher temperatures employed [17,18] (for example, $SrTiO_3$ shows total AO coverage after 72 h of annealing at 1300 °C in air [19]). Additionally, it has been shown that, by employing a combination of polishing and postannealing [20], there is an overwhelming tendency towards AO termination. Surface reconstructions of (001)-terminated perovskites are another clear and present obstacle to the production of pristine surfaces. A well-documented reconstruction on $SrTiO_3$ is composed of TiO_2 structures on a TiO_2 bulk termination [21,22].

Surface formation in perovskites is often more nuanced than a simple comparison of surface energies. For the (001) surfaces of oxide perovskites, both AO and BO_2 terminations are typically considered [23,24], as either can form depending on the chemical conditions employed [25]. Once exposed, the surface can evolve due to changes in chemical potential, leading to compositional shifts through processes such as degradation, adsorption, and vacancy formation [26–31]. Over time, and under favorable conditions, elemental diffusion tends to

*Contact author: n.t.taylor@exeter.ac.uk

†Contact author: s.p.hepplestone@exeter.ac.uk

Published by the American Physical Society under the terms of the Creative Commons Attribution 4.0 International license. Further distribution of this work must maintain attribution to the author(s) and the published article's title, journal citation, and DOI.

occur from regions of high to low concentration [18,32–34], resulting in the formation of atomic vacancies as species precipitate or vaporize to form more stable compounds [35–37]. The stability of a surface is therefore not only determined by its formation energy, but also by its resistance to vacancy formation, which ideally requires a high-vacancy formation energy per unit cell relative to the formation energy of the bulk.

Surfaces may also reconstruct to lower their energy following cleavage [21,22,38–40], yet predicting such reconstructions remains computationally expensive [22,41–43], and first-principles searches are typically limited to small supercells. These difficulties are compounded by the sensitivity of surface stability to the chemical potentials of constituent elements, which vary with synthesis or cleavage conditions [18], and by the possibility of multiple reconstructions coexisting on a single surface [44,45], further complicating the energetic landscape. While global optimization methods have been developed for surface systems [46], they often focus on structural diversity rather than thermodynamic stability. In light of these challenges, examining the role of vacancies in AO- and BO_2 -terminated slabs offers an alternative perspective, providing insight into potential degradation pathways, chemical evolution, and the mechanisms that may underpin surface reconstruction.

Recent machine-learned interatomic potentials have accelerated bulk structure searches [43,47,48], but their transferability to surfaces remains limited, often misidentifying energetic rankings even near the ground state [49]. Fine tuning these models for surface-specific applications is ongoing [49], though it typically requires large, tailored data sets.

In this work, we explore, via first principles, the role of vacancies on surface stability of a set of nine alkaline-earth-metal oxide perovskites (ABO_3, where $A = \mathrm{Ca, Sr, Ba}$ and $B = \mathrm{Ti, Zr, Sn}$). We do so by first considering the energy of formation of the two potential (001) surface terminations, AO and BO_2. We take this discussion further by exploring how the favorability of the two terminations is affected by changes in growth chemical environments. We then study the energetics of A-, B-, and O-site vacancies both in the bulk perovskites, and in slabs as a function of depth.

II. METHODS

A. Computational methods

In this work, first-principles techniques based on density functional theory (DFT) were used to determine the structural and energetic properties of a set of nine oxide perovskites ($CaTiO_3$, $SrTiO_3$, $BaTiO_3$, $CaZrO_3$, $SrZrO_3$, $BaZrO_3$, $CaSnO_3$, $SrSnO_3$, and $BaSnO_3$, hereafter referred to simply as *the perovskites*). These calculations were performed using the Vienna *ab initio* simulation package (VASP) [50,51]. The valence electrons for each atomic species were considered as follows: Ca $3p^6\ 4s^2$, Sr $4s^2\ 4p^2\ 5s^2$, Ba $5s^2\ 5p^6\ 6s^2$, Zr $4s^2\ 4p^2\ 5s^2\ 4d^2$, Ti $3p^6\ 3d^4\ 4s^2$, Sn $5s^2\ 5p^2$, O $2s^2\ 2p^4$. The projector augmented wave method was used to describe the interaction between core and valence electrons, and a plane-wave basis set was used with an energy cutoff of 700 eV. In a heterogeneous system, the presence of multiple substructures with distinct periodic characters necessitates higher plane-wave cutoff to resolve the more complex superposition of basis functions. Unless otherwise stated, calculations were completed using the generalized gradient approximation Perdew-Burke-Ernzerhof (GGA-PBE) functional [52]. All calculations were performed with spin-polarized settings. The PBE functional is chosen for three key reasons: (1) GGA-PBE has been extensively employed previously for oxide perovskite studies [7,53–59], allowing for comparison with this work, and deviations from experiment are, as such, well documented, (2) it shows reasonable geometric accuracy and self-consistency [60–62], and (3) in addition to prohibitive computational cost, more accurate functionals, such as HSE06 [63], are still found to deviate from experiment, in some cases even exhibiting greater inaccuracy than PBE [55], or require exchange fraction fitting [64] and other times showing reliably predictable corrections [65]. For geometrical relaxations, all forces were relaxed to less than 0.01 eV/Å per atom, and electronic self-consistency is accurate to within 10^{-7} eV.

The crystal structures of the perovskites are as follows: $CaTiO_3$, $CaZrO_3$, $CaSnO_3$, $SrZrO_3$, and $SrSnO_3$ are all orthorhombic (space group *Pnma*), $BaTiO_3$, and $SrTiO_3$ are tetragonal (space group $P4mm$), and $BaZrO_3$, and $BaSnO_3$ are cubic (space group $Pm\bar{3}m$). Initial bulk perfect crystals for the perovskites were obtained from the Materials Project database [66,67], with subsequent structural relaxations then performed using VASP (for $SrTiO_3$, the structure relaxes to a tetragonal phase from the cubic one found on the Materials Project). Primitive cells of the orthorhombic perovskites contain four perovskite units ($A_4B_4O_{12}$), whereas tetragonal and cubic perovskite cells contain a single perovskite unit (ABO_3). All considerations of k-point grids are performed using a single cubic perovskite unit as the reference, using $10 \times 10 \times 10$ Monkhorst-Pack grid [68], or equivalents. Both the lattice constants and the atomic positions for the undefected bulk cells are relaxed (cell-free relaxation) to obtain the theoretical ground state. Bulk vacancies are modeled in $2 \times 2 \times 2$ supercells, giving a vacancy concentration of 0.031 and 0.125 vac/unit (average of 4.8×10^{20} and 1.8×10^{21} $/\,\mathrm{cm}^3$) for orthorhombic and tetragonal and cubic crystals, respectively (a representation of the supercells is provided in Fig. S2 in the Supplemental Material [69]). Previous studies have shown a reasonable convergence of supercell size on vacancy formation energy for oxide perovskites [60]. Further details regarding the lattice constants, phases, structural setup, and calculated band gaps of the bulk materials are provided in Secs. SII A and SIII A and Table SIII [69]. For bulk vacancy calculations, cell-free relaxation is performed (see Sec. SIII B [69] for further details).

A *slab* is a thin film of a material bordered by vacuum either side and is used to model surfaces in computational studies. It consists of a sufficiently large number of atomic layers to ensure that the central layers retain bulklike properties, while still allowing for surface effects to be studied. In this work, the term *slab* refers to the entire structure, while *surface* specifically denotes the outermost atomic layer (top layer) of the slab. The layer immediately beneath the top layer is referred to as the *subsurface*, and all deeper layers are labeled according to their layer number, as shown in Fig. 1. For each perovskite, the (001) AO- and BO_2 -terminated slabs were generated using ARTEMIS [70].

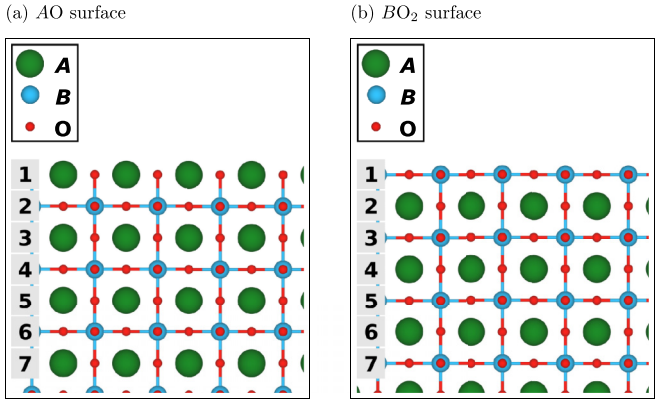


FIG. 1. Ball-and-stick representation of the two (001) surface terminations of a tetragonal (and cubic) oxide perovskite: (a) AO and (b) BO_2. While the orthorhombic phase exhibits slight tilting, these two terminations are the only unique (001) surfaces, with minor distortions to the structure. Layer 1 is defined as the *surface* layer, layer 2 is the *subsurface* layer, and all other layers are referred to using their respective numbers as labeled in the figure. Figure generated using VESTA [81].

AO-terminated (BO_2 -terminated) slabs include six layers of complete units of ABO_3, with an additional layer of AO (BO_2) to result in two symmetrically equivalent surfaces on the slab. A 14-Å vacuum gap is introduced along the [001] Miller direction to separate the two surfaces of a slab. The slab surfaces are then extended to retrieve 2×2 ($\mathbf{a} \times \mathbf{b}$) extensions (for further details, see Sec. SII A [69]). Vacancies in slabs are modelled on the 2×2 supercells, with six layers of perovskite units, resulting in vacancy concentrations of 0.021 and 0.042 vac/unit (average of 7.7×10^{13} and $1.5 \times 10^{14}\,\mathrm{cm}^{-2}$) for orthorhombic and tetragonal and cubic crystals, respectively (a representation of the slabs is provided in Fig. S2 in [69]). For undefected and defected slab calculations, the cell is fixed while atomic positions are relaxed (fixed-cell relaxation).

In real materials, vacancy defects can adopt different charge states, which are balanced by the surrounding environment. The influence of charge states on defect formation energies in $SrSnO_3$ is investigated by explicitly modeling charged vacancies for a range of charge states. Specifically, the following charge states are considered: V_{Sr} -3 to $+3$, V_{Sn} -4 to $+3$, and V_O -2 to $+2$. While, in bulk materials, these defects are known to take on particular charge states, it is unknown what effect a nearby surface will have on the available charge states and, thus, a wider range than typical is explored.

Defect calculations are performed using a fixed-cell approach, where the lattice constant is constrained to its bulk value, allowing atomic relaxations while maintaining a consistent dielectric background. This is necessary to properly account for image charge interactions between periodic images. The force and energy convergence criteria for charged defect calculations are consistent with those outlined above for noncharged calculations. The respective charge-neutral bulk vacancies are recalculated using fixed-cell relaxation, as required by the correction methods. The difference between the cell-free and fixed-cell charge neutral vacancies for $SrSnO_3$ is 0.03 eV/vac.

A comparison of the formation energies of surfaces and neutral charge defects within oxide perovskites for machine-learned potentials versus DFT is presented in Sec. SII G [69], where it is found that these models, while able to accurately capture the energetic ordering of their (001) surfaces, is wholly unable to capture energetic trends of bulk and near-surface vacancies. As such, without further training, these models are not applicable to the space of vacancies in oxide perovskites.

Corrections to the formation energies of bulk charged defects are applied using `doped` [71], which implements the extended Freysoldt, Neugebauer, and Van de Walle (eFNV) method [72] to mitigate finite-size effects arising from periodic boundary conditions. For charged defects in slab geometries, the `qdef2d` [73] and `sxdefectalign2d` [74,75] packages are used to automate the application of appropriate correction schemes for systems that include vacuum regions. The total relative dielectric values used for $SrSnO_3$ are $\varepsilon_{r,xx} = 18.239$, $\varepsilon_{r,yy} = 18.850$, and $\varepsilon_{r,zz} = 16.329$, with all other values set to 0 (obtained from the Materials Project [66]. For slab calculations, the c axis is parallel to the surface normal vector, meaning that the dielectric constant along the slab is $\varepsilon_{r,zz}$. While a permittivity of a slab should be calculated directly, this has a high associated computational cost; as it is known that permittivity reduces for thin films [76], the choice of the bulk dielectric values can be taken as the upper limit. The method employed for studying image charges and the associated correction methods are discussed exhaustively in Refs. [72,75,77].

To address inaccuracies in band gap and band alignment inherent to the GGA-PBE functional, additional calculations are performed using the HSE06 hybrid functional [63] in a *one-shot* approach. For the undefected bulk and AO- and BO_2 -terminated slabs of $SrSnO_3$, a single self-consistent calculation is carried out on GGA-PBE-relaxed structures to obtain more accurate electronic and energetic properties. These refined values are then incorporated into the defect calculations using the averaged electrostatic potential-referenced band-edge shift (BES) method [78] to further improve accuracy. While HSE06 does not accurately capture the experimental band gap of $SrSnO_3$, it is an improvement from GGA-PBE, thus providing more qualitatively meaningful results.

B. Surface formation energy

In order to compare the energetics of different surface terminations, we require a surface formation energy for each. Formation energies are used to compare the energetic favorability of elements in different compounds or phases. For this work, we consider two approaches for defining energetic surface stability. The first is for simple comparisons based upon taking the relevant binary oxides (AO and BO_2) as references. The second approach uses the generally more in-depth evaluation involving chemical potentials. For the first, we use the ABO_3 perovskite, and the AO and BO_2 binary oxides as comparison compounds, due to their stability and favorability in oxygen-rich environments [79,80] (see Table SIV [69]). Energy values, E_X, denoted here correspond to a DFT calculated total energy of one chemical unit of the X

compound. Finally, for surfaces, formation energy is given per unit surface area, which makes the value independent of surface supercell employed.

The equation used to calculate surface formation energy for a particular slab is

$$E^i_{\text{form}} = \frac{\left[E^i_{\text{slab}} - N^i_{ABO_3}E^{\text{bulk}}_{ABO_3} - N_{i\text{-ox}}E^{\text{bulk}}_{i\text{-ox}}\right]}{2A}, \quad (1)$$

where $E^{\text{bulk}}_{ABO_3}$ is the energy of the bulk perovskite, E^i_{slab} is the energy of the perovskite slab with surface termination i, $N^i_{ABO_3}$ is the number of complete units of ABO_3 in the slab, and $E^{\text{bulk}}_{i\text{-ox}}$ and $N_{i\text{-ox}}$ are the energy and number of additional units of the i-corresponding binary oxide (AO or BO_2). A is the area of the surface present in the cell (an additional 2 is included to account for there being two symmetrically equivalent surfaces in the cell).

C. Surface Gibbs free energy

While Eq. (1) provides an easy comparison of the data, it does not take into consideration the chemical environment in which the surface is formed. To account for this surface Gibbs free energy must be used. The method used to assess surface Gibbs free energy follows the method outlined by Heifets *et al.* [25] and is provided in further details in Sec. SII C [69].

We can identify the most energetically favorable surface at different chemical conditions (defined by the chemical potentials μ) as the one with the lowest surface Gibbs free energy. The surface Gibbs free energy per unit cell for an i-terminated slab, Ω^i, is defined as

$$\Omega^i = \tfrac{1}{2}\left[G^i_{\text{slab}} - N^i_A\mu_A - N^i_B\mu_B - N^i_{\text{O}}\mu_{\text{O}}\right], \quad (2)$$

where G^i_{slab} is the Gibbs free energy of the slab, N^i_A, N^i_B, N^i_{O} are the number of A, B, and O atoms in the slab, respectively, and μ_A, μ_B, μ_{O} are the chemical potentials of the A, B, and O species, respectively. Halving the first term accounts for the two symmetrically equivalent surfaces present in the slab.

As the system is in equilibrium with the bulk ABO_3, we can show that the chemical potential of the perovskite is interdependent on the chemical potential of its three constituent elements

$$\mu_{ABO_3} = \mu_A + \mu_B + 3\mu_{\text{O}}. \quad (3)$$

We approximate the chemical potential of the perovskite to its Gibbs free energy ($G^{\text{bulk}}_{ABO_3}$), which we define as the DFT energy relating to one chemical unit of ABO_3:

$$\mu_{ABO_3} \approx G^{\text{bulk}}_{ABO_3} \approx E^{\text{bulk}}_{ABO_3}. \quad (4)$$

As μ_{ABO_3} is considered a fixed value, and the chemical potentials (e.g., relative concentrations, temperatures) of A, B, and O are interdependent, there exist only two truly independent variables: we choose these to be those for A and O. We choose to redefine the number of B atoms in terms of a difference in its number compared to A and O atoms (denoted using X),

$$\Gamma^i_{B,X} = \frac{1}{2}\left(N^i_X - N^i_B\frac{N^{\text{bulk}}_X}{N^{\text{bulk}}_B}\right). \quad (5)$$

$\Gamma^i_{B,\text{X}}$ is the number of excess atoms of species X, in i-terminated slab, with respect to the number of atoms of species B. These Γ factors allow us remove the $\Delta\mu_B$ dependency from surface Gibbs free energy Ω^i, allowing us to more clearly consider the effects of different growth and environmental conditions.

Next, we shift the zero of the chemical potentials of species A and O (μ_X) to their bulk energies ($\Delta\mu_X$) which are A bulk and O_2 molecule, respectively. Now we can repostulate the surface Gibbs free energy from Eq. (2) in terms of merely the chemical potential of the two species A and O, with that of species B being wholly dependent on A and O:

$$\Omega^i = \phi^i - \Gamma^i_{B,A}\Delta\mu_A - \Gamma^i_{B,\text{O}}\Delta\mu_{\text{O}}, \quad (6)$$

where

$$\phi^i \approx \tfrac{1}{2}\left[E^i_{\text{slab}} - N^i_B E^{\text{bulk}}_{ABO_3}\right] - \Gamma^i_{B,A}E^{\text{bulk}}_A - \tfrac{1}{2}\Gamma^i_{B,\text{O}}E_{O_2}, \quad (7)$$

and E^{bulk}_A (E_{O_2}) is the energy of an individual A atom in its bulk (individual O atom in an O_2 molecule). We can now vary the relative chemical potentials, $\Delta\mu_A$ and $\Delta\mu_{\text{O}}$, to find the formation energy of each material at different environmental conditions; for a set of chemical potentials ($\Delta\mu_A$ and $\Delta\mu_{\text{O}}$) the material with the lowest formation energy Ω^i is the most energetically favorable material at that chemical condition.

D. Vacancy formation energy

To calculate the formation energy of a vacancy in the bulk, we use the binary oxides as the relative compounds for comparison (i.e., determine whether the vacant atom would prefer to reside in the perovskite bulk or in its corresponding binary oxide):

$$E^{\text{bulk}}_{\text{form},X} = \left(E^{\text{bulk}}_{X\text{-vac}} + E^{\text{bulk}}_{X\text{-ox}}\right) - \left(N_{\text{cells}}E^{\text{bulk}}_{ABO_3} + \frac{N^X_{\text{O}}}{2}E_{O_2}\right). \quad (8)$$

Here, $E^{\text{bulk}}_{X\text{-vac}}$ is the energy of the vacated perovskite bulk supercell, $E^{\text{bulk}}_{X\text{-ox}}$ is the energy of the X-based binary oxide, N_{cells} is the number of perovskite units in the undefected supercell, E_{O_2} is the energy of an isolated O_2 molecule, and N^X_{O} is the number of oxygen atoms in the chemical unit of the X-based binary oxide.

Formation energies for vacancies in the slab are given with respect to the corresponding bulk vacancy

$$E^i_{\text{form},X} = \left(E^i_{X\text{-vac}} + N_{\text{cells}}E^{\text{bulk}}_{ABO_3}\right) - \left(E^i_{\text{slab}} + E^{\text{bulk}}_{X\text{-vac}}\right), \quad (9)$$

where $E^i_{X\text{-vac}}$ is the energy of the vacated slab with surface termination i. Clearly, Eq. (8) depends on choice of chemical potentials. However, for vacancies in slabs, we are more interested in the favorability of a vacancy as a function of depth and, as such, Eq. (9) allows us to focus solely on this, avoiding the issue of an arbitrary choice of chemical potential.

For the nine perovskites, there exists one symmetrically unique A site and one B site. For the tetragonal and cubic perovskites, there exists one symmetrically unique O site. However, for the orthorhombic perovskites, there exist two inequivalent O sites, the 4c and 8d Wyckoff positions. Vacancies have been explored in the bulk on both sites, but only the most energetically favorable site is presented in this work (see Sec. SIII B in [69] for further details). For the slab

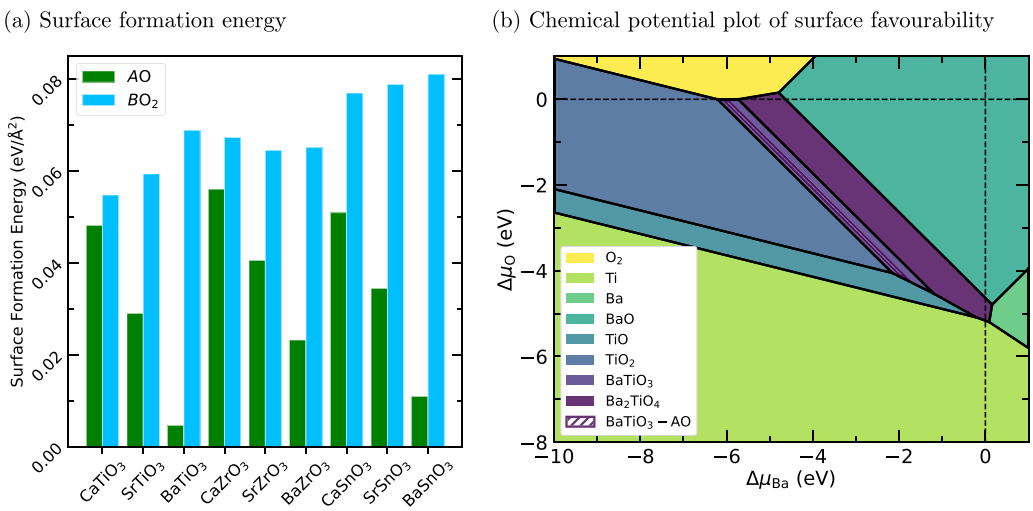


FIG. 2. Relative stability of ternary oxides and constituents. (a) The surface formation energy for nine oxide perovskites (ABO_3) terminated on the (001) plane with either their AO and BO_2 surface. The formation energies for the AO- and BO_2 -terminated slabs are given with respect to the composite binary oxide, AO and BO_2, respectively. (b) Chemical potential plot for $BaTiO_3$, following the method outlined in [25]. The chemical potential values of Ba and O are varied, with that of Ti being inherently linked to the others by the chemical formula $BaTiO_3$. Note, the surfaces are never more favorable than the undefected bulks, so denote where the surfaces would form if the perfect crystal did not exist using a hashed region. The BO_2 termination does not appear on the chemical potential plot as it is never more favorable than the other compounds present.

vacancies, all symmetrically inequivalent sites are explored for all vacancies.

III. RESULTS AND DISCUSSION

A. Clean (001) surfaces

To understand perovskite surfaces, we first explore clean slabs terminated on the (001) Miller plane [see Fig. 1 for a representation of the two (001) surface terminations, AO and BO_2]. We examine the surface formation energy, which allows us to understand the relative stability of each surface. Higher formation energies correspond to a less energetically favorable surface while lower formation energies correspond to a more favorable or more easily formed surface. A negative surface formation energy indicates that spontaneous surface formation occurs and the bulk material is energetically unstable. The formation energies for the two potential (001) surface terminations (AO and BO_2 terminated) of the nine oxide perovskites are shown in Fig. 2(a); here, the values are given relative to composite binary oxides (AO and BO_2) and the bulk perovskite (ABO_3) are presented in Fig. 2(a). All the surfaces' formation energies are positive [see Fig. 2(a)], which highlights that spontaneous formation of (001) surfaces does not occur and, as such, the bulk systems can be considered energetically stable.

We find that, in all perovskites considered, the AO surface is more energetically favorable than their corresponding BO_2 surface; this agrees with experimental works that have shown a preference for $SrTiO_3$ and 3,3 perovskites to form the AO surface when first grown [18,20]. From considering both Fig. S4 [69] and Fig. 2(a), it is clear that the phase of the perovskite is unrelated to which surface is more favorable. For Ca-based oxide perovskites ($CaBO_3$), AO and BO_2 surfaces are the closest in formation energies. As we change period of the A-site ion, the formation energies of the AO and BO_2 surfaces diverge, with Ba-based oxide perovskites ($BaBO_3$) exhibiting the largest differences. These two surface types show opposite trends for their formation energies. For AO surfaces within a particular B ion (e.g., group IV perovskites, $ATiO_3$), the formation energy decreases as the A ion increases in period. For BO_2 surfaces, the formation energy either remains relatively constant, or increases slightly with increasing period of the A-site ion within group II.

We also perform a study of the favorability of the two surfaces for different chemical environments and find that the AO-termination preference holds for almost all environments (i.e., different temperatures, pressures, and elemental concentrations). Figure 2(b) shows that, for $BaTiO_3$, the AO surface is the only (001) termination to be more stable than its composite binary oxide compounds for any set of chemical potential values (all nine perovskites are presented in Fig. S9 [69] and generally hold to this trend); this agrees with what has previously been seen for $BaTiO_3$ and $BaZrO_3$ [25,82]. This is of particular interest for systems such as $SrTiO_3$, which have shown both surfaces experimentally [15]. For further details regarding the generation of these chemical potential plots, see Sec. SIII F [69].

The universal energetic favorability of AO surfaces over the corresponding BO_2 surface is ascribed to a more significant change in surface charge in the AO surface than the BO_2. The charges on the oxygen atoms at the AO surface are found to lie closer to their ideal oxidation number of -2 than at the BO_2 surface. The oxidation number of -2 represents a full outermost orbital on the oxygen atoms. Therefore, oxidation numbers closer to -2 are more energetically favorable than numbers closer to -1, such as on the BO_2 -terminated surface.

We suggest that the general trend of decreasing surface formation energy with higher A-site atomic number can be attributed to the decreasing first and second ionization energy with increasing period (see Fig. S1 [69]). As the A-site cation

TABLE I. Chemical potential limits for the oxygen-rich environment for each oxide perovskite. The chemical potential values are given with respect to the elemental reference phases, i.e., *A* and *B* bulk metals and O_2 gas.

	Chemical potential (eV)		
O-rich limit	*A* site	*B* site	O site
$CaTiO_3$-TiO_2-O_2	−6.62	−9.20	0.00
$SrTiO_3$-TiO_2-O_2	−6.59	−9.20	0.00
$BaTiO_3$-TiO_2-O_2	−6.21	−9.20	0.00
$CaZrO_3$-ZrO_2-O_2	−6.29	−10.37	0.00
$SrZrO_3$-ZrO_2-O_2	−6.24	−10.37	0.00
$BaZrO_3$-ZrO_2-O_2	−6.12	−10.37	0.00
$CaSnO_3$-SnO_2-O_2	−6.33	−5.10	0.00
$SrSnO_3$-SnO_2-O_2	−6.18	−5.10	0.00
$BaSnO_3$-SnO_2-O_2	−5.93	−5.10	0.00

period increases, the shielding and distance of the electrons with respect to the nucleus also increases, resulting in a lower ionization energy than elements with a smaller period in the same group. Although the total amount of charge redistributed from each *A*-site ion is roughly equal, the energetic cost of removing these electrons from an *A*-site decreases with increasing period, and, as such, they are energetically cheaper to donate.

We compare the energies of perovskites with the same *A*-site cation, but with different *B*-site ions. For *A*O-terminated slabs, we find similar formation energies between them. For example, Ca*B*O_3 formulas have an *A*O surface formation energy of approximately 0.051 ± 0.003 eV/Å^2, Sr*B*O_3 have an *A*O surface formation energy of roughly 0.036 ± 0.007 eV/Å^2, and Ba*B*O_3 have *A*O surface formation energies of roughly 0.013 ± 0.009 eV/Å^2.

Overall, we see little change in formation energy for *A*O-terminated slabs when the *B*-site cation is changed and, similarly, little change in formation energy for BO_2-terminated slabs when the *A*-site cation changes period. This is not unexpected as the surface cation should be the dominant contributor to the change in surface formation energy. In addition, we suggest that the reason for the titanate BO_2 surface formation energy increasing with respect to increasing *A*-site period is that the Ti ion has significantly fewer core electrons than Zr and Sn. This in turn means that it has less core screening. As such, changing *A*-site cation more strongly affects the bonding of Ti-O than it would for Zr-O and Sn-O.

B. Neutral vacancies in the bulk

Before considering the role of vacancies at a surface, we first explore the energetics of *A*, *B*, and O vacancies in bulk. Figure 3 shows the energy of formation of *A*-, *B*-, and O-site vacancies in bulk, given in an O-rich environment (i.e., the *AB*O_3-BO_2-O_2 limit); this choice is made due to the abundance of oxygen within the atmosphere and, thus, the likely condition to find these perovskites in. The values for the chemical potentials used are presented in Table I. In Fig. S4 [69], we also considered these vacancies with respect to the bulk binary oxides and the bulk metals. Under oxygen-rich conditions, the *A*-site vacancies are always the most favorable vacancy. *B*-site and O-site vacancies are similar in energies, with O-site vacancies being more favorable in $ASnO_3$, less favorable in $AZrO_3$, and comparable energies in $ATiO_3$. This ordering can be changed based on the choice of comparison compounds (such as comparing to the *A* and *B* bulks or their binary oxides). Note, when considering these vacancies against forming the bulk metal, the O-site vacancies become more favorable, but these energies are substantially higher than with respect to the oxides. When comparing to the binary oxides, the *A*-site vacancy is always found to be the most favorable vacancy, *B*-site the second, and *O*-site the least favorable vacancy.

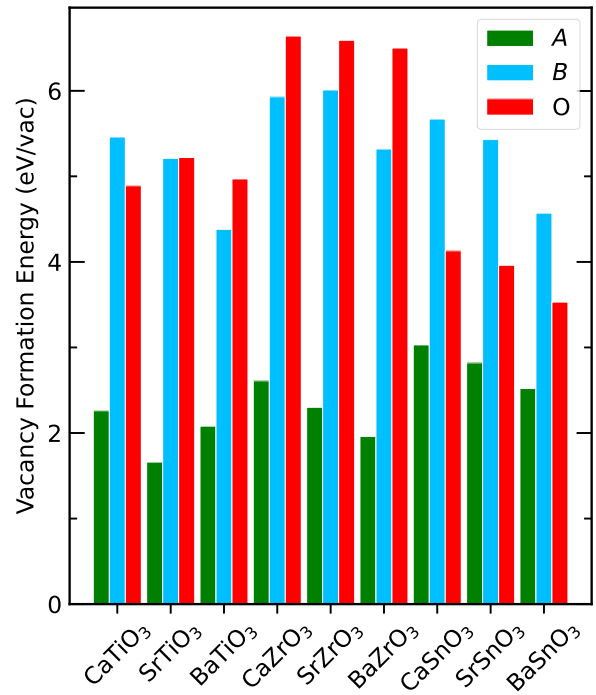


FIG. 3. The formation energy of different *A*-, *B*-, and O-site vacancies in various oxide perovskite (*AB*O_3) bulk crystals (evaluated in the O-rich limit, see Table I). For the orthorhombic-phase perovskites, the O-site corresponding to the lowest-energy vacancy is presented; for $CaTiO_3$, $SrZrO_3$, and $CaSnO_3$, this is the 4*c* Wyckoff position, while for $CaZrO_3$ and $SrSnO_3$, it is the 8*d* position.

Our results compare well with literature values for titanate-based perovskites [83–85]: our results and literature both show the formation energies of bulk (or deep level) O-site vacancies in titanate-based perovskites to fall within the range of 5–6 eV. In general, the vacancy formation energy results indicate that *A*-site ions are more likely to vacate the bulk under O-rich conditions than the *B*-site ions.

Our results show that, within a certain *B*-based compound (i.e., titanates, zirconates, or stannates), both all vacancy sites exhibit a decreasing formation energy with increasing *A*-site period (with the exception of $SrTiO_3$ for *A* sites, $SrZrO_3$ for *B* sites, and $CaTiO_3$ for O sites).

All vacancies show similar comparability between *B*-site groupings, with the exception of oxygen vacancies in zirconates. Within materials of the same *A* site, stannates show the smallest variation in vacancy formation energy of different defects (∼3.1 eV). Titanates show a larger variation in

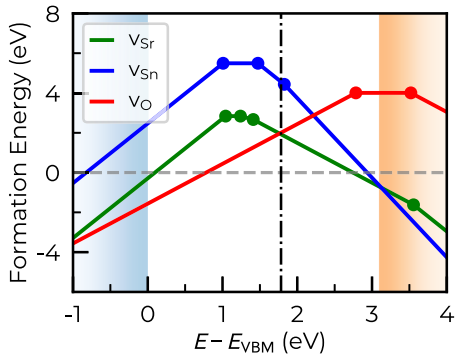


FIG. 4. Formation energies of *A*-, *B*-, and O-site charged vacancies in bulk $SrSnO_3$ (evaluated in the O-rich limit, see Table I). Line gradients correspond to the charge state (in $|e|$) and points of discontinuity identify transition levels. The valence (conduction) band region is shaded in blue (orange) and the vertical dashed-dotted line is the equilibrium Fermi level. Corrections to the charge state energies are calculated using DOPED [71], which employs band-edge shifting [78] and image charge corrections [72].

formation energy (∼3.8 eV), and zirconates show the largest variation in vacancy formation energy (∼4.6 eV). The oxygen vacancy formation energy of zirconates is about 2 eV higher than in the stannates or titanates, where all other vacancy energies are more consistent.

C. Charged vacancies in bulk $SrSnO_3$

The transition levels of charged vacancies for $SrSnO_3$ are presented in Fig. 4 for the O-rich limit ($SrSnO_3$-O_2-SrO). $SrSnO_3$ is chosen as the example oxide perovskite for charge state studies for three reasons: (1) prior literature studies of charged defects in bulk [86,87], (2) it shows the least structural distortion brought on by introducing vacancies (see Sec. SIII H in [69]), and (3) it shows reasonable convergence of vacancy energies to their bulk counterparts in both surface terminations [see Fig. 5(c)]. The theoretical band gap for $SrSnO_3$ bulk is calculated as 3.09 eV using HSE06.

The charge-neutral defect formation energies align with those presented in Fig. 3. Additional plots are presented in Fig. S10 [69] for different chemical potential limits. Under the same chemical environment (see Fig. S6 in [69]), the charged defects agree with those presented in Ref. [86]; the band gap is in disagreement due to the choice of mixing employed by the hybrid functional (this study uses the default parameters of HSE06).

The O $(+2/0)$ is a shallow defect, along with O $(0/-2)$ and Sr $(-2/-3)$ that fall above the conduction band minimum. The other Sr and Sn transitions are deep level transitions, sitting near the middle of the band gap. In this oxygen-rich limit, the pinned Fermi level sits at 1.78 eV above the valence band maximum (VMB); see Table SXII [69] for Fermi level under different chemical conditions. The formation energy of the charged defects lies above 0 eV for most of the band gap, i.e., 0.5–2.5 eV.

The dopability of $SrSnO_3$, in agreement with literature [86,87] (and other oxide perovskites [88]), is found to be *n*-type dominated with oxygen vacancies under the SnO-$SrSnO_3$ -Sn limit than *p*-type oxygen vacancies under O-rich conditions (see Sec. SIII I in [69]). This is the case because a higher formation energy for defects at the band edges suggests a system that is more stable to those vacancies, so can support more. The dopability limit in the O-rich condition lies from 0.50–2.47 eV, showing a range for the Fermi level of 1.97 eV.

D. Neutral vacancies at surfaces and in slabs

We now evaluate the role of vacancies in slab structures. For clean surfaces, we have shown that, based on arguments for the surface formation energies for all the unvacated slabs, the BO_2 surfaces are highly unfavorable and unlikely to occur.

We have investigated, for the nine oxide perovskite considered here, the role of *A*-, *B*-, and O-site vacancies as a function of depth from the surface (i.e., layer number). In Fig. 5, we show the formation energy of the various vacancies considered. The vacancy formation energies presented show how much more (or less) energetically favorable these surface vacancies are compared to the bulk. Our results show that the vacancies in the surface layer are more favorable than in bulk, in agreement with previous first-principles studies that have observed the same surface preference of vacancies in $ATiO_3$ perovskites and metal [84,89]. This trend indicates that for all the perovskites, one can expect higher concentrations of vacancies at the surface than in the bulk. Our results also agree with the expectation that the vacancy formation energies (with respect to the bulk vacancy) tend towards zero as they approach the deepest point in our simulated slabs (i.e., tend to the bulk vacancy result). In general, this trend of vacancy formation energy converging to the bulk value is followed by *AO* surfaces more so than BO_2 surfaces which have a number of exceptions. In many of the structures, we observe an oscillation of oxygen vacancy formation energies between the *AO* and BO_2 layers. This has previously been reported for $SrTiO_3$ slabs [90,91], but we show that this can be generalized to further perovskites, as seen in Fig. 5.

The *A*- and *B*-site surface vacancies are more energetically favorable than in bulk by approximately 1.6 and 1.9 eV, respectively. Due to this high-energy preference of surface vacancies to those in bulk, defect density at the surface will be substantially higher than in the bulk (by several orders of magnitude). As mentioned earlier in this work, for bulk formation energy, we see that, in all perovskites presented here, the *A*-site bulk vacancies are the most energetically favourable, with a formation energy of around 3.2 eV whereas the average *B*-site bulk vacancies are 4.5 eV. This results in *A*-site and *B*-site vacancies at the surface with formation energies of around 1.6 and 2.7 eV. Therefore, *A*-site vacancies are more favorable at *AO*-terminated surfaces than *B*-site vacancies at BO_2-terminated surfaces. As most distribution functions (such as Boltzmann) have an exponential tendency for these energies, this results in substantially more *A* vacancies in a *AO* surface than *B* vacancies in a BO_2 surface. Hence, *AO* surfaces, while more energetically favorable, are more prone to vacancies and, as such, are likely easier to degrade, revealing a BO_2 layer below. We provide an individual breakdown of these analyses for each perovskite in Sec. SIII G in [69], but the trend holds.

While the *A* and *B* vacancies' trends are clear to understand, the oxygen vacancies show the most variation in their

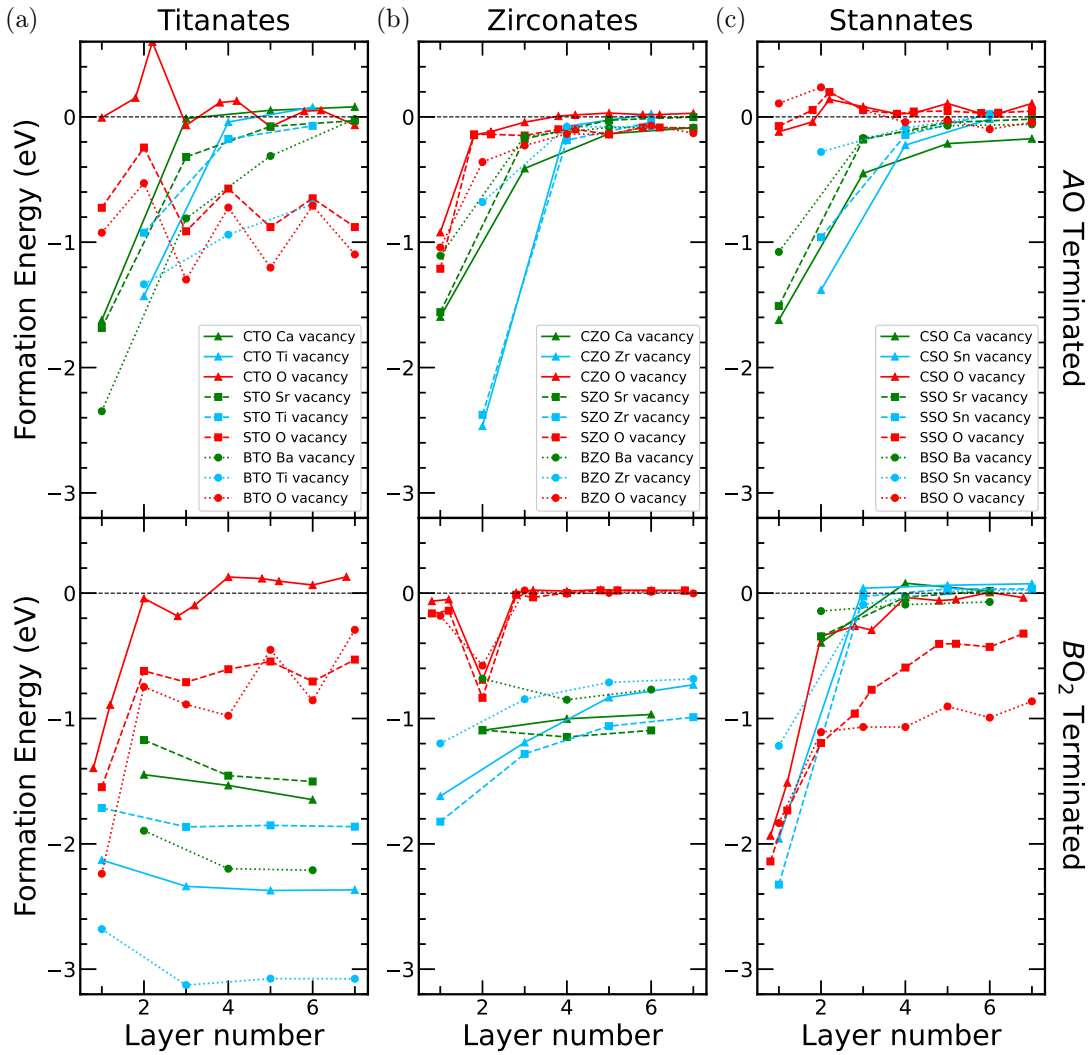


FIG. 5. Formation energies of *A*-, *B*-, and, O-site vacancies within (a) titanate, (b) zirconate, and (c) stannate oxide perovskites, as a function of layer depth from the surface. The upper (lower) panels show vacancies in *AO*- (BO_2-) terminated slabs. Vacancy formation energies are given with respect to the vacancy formation energies in bulk, as seen in Fig. 3. For reference, we note that the *A* vacancies in bulk are generally much more energetically favorable than the *B* vacancies in bulk. For systems that exhibit a tilt (i.e., orthorhombic phases), there exist two unique oxygen sites in the BO_2 layers, one lying slightly above the *B*-site plane, and one slightly below. To distinguish between these two O sites, they have been presented at 0.2 above and below the corresponding *B* layer number.

behavior. We noted earlier that the formation energies of these oscillate between *AO* and BO_2 layers, but our results show that this trend is reduced for zirconate systems, and for these zirconates, oxygen vacancies are more favorable in *AO* surfaces, whereas, in the stannates and titanates, the BO_2 surfaces are more favorable.

There are a few anomalies to note: $CaTiO_3$ oxygen vacancies in both *AO*- and BO_2-terminated slabs have higher formation energies than their other titanate counterparts (where $CaTiO_3$ O-site vacancies converge to the bulk value, whereas $SrTiO_3$ and $BaTiO_3$ O-site vacancies converge to a value approximately 0.5 eV below their bulk values). This is likely linked to the $CaTiO_3$ phase being orthorhombic, while $SrTiO_3$ and $BaTiO_3$ are tetragonal. $BaSnO_3$ O-site vacancies in the BO_2-terminated slab has a similar energy shift, which is the only cubic phase stannate, when compared to $CaSnO_3$ and $SrSnO_3$, which are orthorhombic. When studying the $BaSnO_3$ BO_2 oxygen vacated slabs, we find that the relaxed structure exhibits an orthorhombiclike phase, with the *B*-O substructure becoming tilted (see Sec. SIII H in [69]).

One final anomaly with the results is that *A*- and *B*-site vacancies in BO_2-terminated titanates and zirconates converge to energies below the respective vacancy formation energy in bulk. In Table SVIII in [69], we highlight how the O–*B*–O bonds become distorted in these structures to a polar phase of the perovskite structure, which is more energetically favorable than the nonpolar system. Polarization due to the presence of vacancies has previously been observed in DFT studies of $SrTiO_3$ [91].

Aside from the exceptions detailed previously, there is a general trend, in particular for cations, for the vacancy formation energy to be lowest in the first two layers of the material. More negative vacancy formation energies compared to bulk implies that the material is susceptible to physical

(a) Charge defects in AO slab, O-rich limit (b) Charge defects in BO_2 slab, O-rich limit

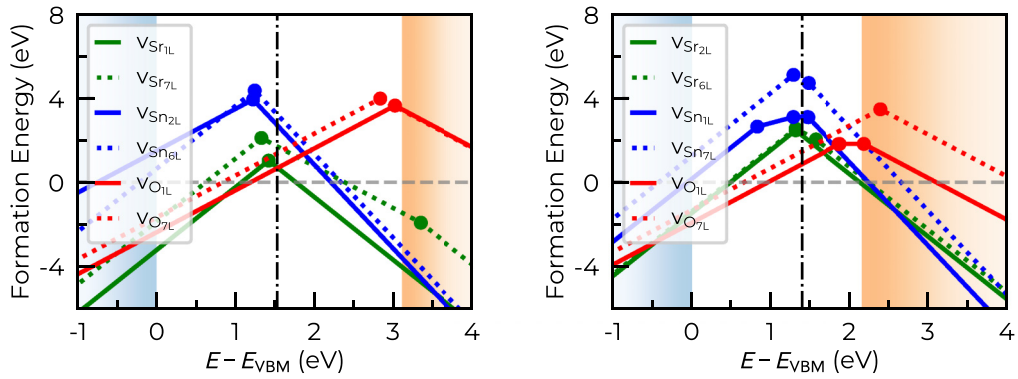


FIG. 6. Formation energies of A-, B-, and, O-site charged vacancies in $SrSnO_3$ (a) AO- and (b) BO_2-terminated slabs under O-rich conditions (see Table I). Line gradients correspond to the charge state (in $|e|$) and points of discontinuity identify transition levels. The valence (conduction) band region is shaded in blue (orange) and the vertical dashed-dotted line is the equilibrium Fermi level. Corrections to the charge state energies are calculated using the following codes: `doped` [71], `qdef2d` [73], and `sxdefectalign2d` [74,75], which employ band-edge shifting [78], image charge [72], and slab charge [74,75] corrections.

degradation, therefore deeming the surface unstable. This corroborates the results of recent experimental findings for $SrTiO_3$ where all surfaces contained both BO_2 and AO terminations [15,16], presumably, in part, due to the fact that degradation of one layer will reveal the preceding layer. The phenomenon of Sr segregation on the (001) surface for $SrTiO_3$ has also been demonstrated through long annealing times at temperatures of around 1300 °C [19]. This seems to be in agreement with our results showing that vacancies are more favorable at the surface than in bulk. It is common for vacancies to form during sample manufacturing [92], annealing at high temperature would increase the rate of vacancy diffusion into the material resulting in Sr precipitation at the surface.

E. Charged vacancies at $SrSnO_3$ surfaces and in slabs

The concentration and stability of vacancies depend on their charge states, governed by the Fermi energy. While bulk charge states in oxide perovskites are well studied [86], surface influence remains less explored. Prior studies on perovskite stannates have focused on fully ionised cation vacancies, such as V_{Sr}^{-2} and V_{Sn}^{-4} in $SrSnO_3$. Since no specific dopant environment is assumed, we examine a range of compensating vacancies, including those deviating from expected ionized charge states. Given the interest in both p- and n-type doping for stannate perovskites [86,88], a comprehensive defect study is necessary.

We analyze how surface termination affects charged vacancy states in $SrSnO_3$ (see Fig. 6). We note at the beginning that, overall, charge defects still support A-site vacancies being dominant. Charge states are explored under the oxygen-rich limit (see Figs. S11 and S12 in [69] for variations in chemical potential). In both AO- and BO_2-terminated slabs, charge states at the center resemble the bulk, but being shifted 0.5–1 eV toward the valence band (more significantly for the BO_2-terminated slab). Most charge states either remain bulklike or become more stable at the surface, except for Sn vacancies in the AO-terminated slab due to charge state crossings. This aligns with Fig. 5, which shows that the AO surface further reduces vacancy formation energy. Local potential analysis indicates positive (negative) charges localize around anion (cation) vacancies, while negative (positive) charges delocalize for anion (cation) vacancies.

The BO_2 surface exhibits a reduced theoretical band gap (2.17 eV) relative to the bulk (3.09 eV) [7], whereas the AO surface retains a bulklike gap (3.11 eV). In the bulk, most vacancies have positive formation energies, but this is not the case for slabs. To discuss this, we focus on the oxygen-rich condition. At both the AO and BO_2, the surface Sr (A site) and O vacancies are dominant for the entire band gap (subsurface Sr for the BO_2 surface). For the AO surface, Sr vacancies exhibit negative formation energies across most of the band gap and O vacancies nearer to the valence band, making AO surfaces highly susceptible to vacancies. At the BO_2 surface, it exhibits a much wider range of energies over which no native charged defect has a negative formation energy; oxygen has negative formation energies near the valence bands, comparable to the AO surface, and Sr subsurface vacancies become favorable just at the conduction band minimum. Both surface show a clear preference to Sr (sub)surface vacancies, highlight a likely degradation of the AO surface. For both terminations, V_O is typically the only shallow donor, except for slab center V_{Sr} in AO-terminated slabs, with no native shallow acceptors observed. Overall, both (001) surfaces are less stable than the bulk due to lower vacancy formation energies at the surface. The order of vacancy favorability changes with chemical environment, explored further in Sec. SIII J [69]; one key result is that there exists only one limit in which Sn (sub)surface vacancies are more favorable than Sr (sub)surface vacancies, further supporting the preference towards A-site vacancies near the surface.

Regarding dopability limits, the range within the band gap that can support dopants without forming compensating native vacancies, the AO- and BO_2-terminated slabs exhibit ranges of 0.57 eV (1.19–1.76 eV) and 1.18 eV (0.96–2.14 eV), respectively. With a smaller band gap (2.17 eV), the BO_2 surface's Fermi level dopability range is closer to the band edges, mak-

ing it more stable under doping. This supports the argument that *A*-site vacancies dominate at the *A*O surface, while *B*-site vacancies are less prevalent at the BO_2 surface, indicating greater chemical stability.

IV. CONCLUSION

Our results show that for the (001) termination, *A*O surfaces of the perovskites considered are much more favorable than BO_2 surfaces, despite both being observed experimentally. We propose that BO_2 surfaces, while less energetically favorable, are likely to form from *A*O surfaces that degrade through vacancy formation, exposing the subsurface BO_2 layer. *A*-site vacancies are found to be roughly 1 eV more favorable at *A*O surfaces than *B*-site vacancies at the BO_2 surface, meaning that BO_2 surfaces are more stable against degradation under vacancy formation than *A*O surfaces. In the bulk perovskites examined under O-rich conditions, *A*-site vacancies were found to almost always be the most favorable, with O-site vacancies always being the least favorable. Surface and shallow vacancies show a dominant trend of increasing formation energy with increasing vacancy depth. A number of notable exceptions are discussed. Phase diagrams agree with surface formation energy analysis; for all perovskites studied, under conditions when bulk ABO_3 is sustainable, the only stable (001) surface is the *A*O, with the exceptions of $CaTiO_3$ and $CaSnO_3$. The former shows both *A*O and BO_2 to exist, while the latter has no stable *A*O or BO_2 (001) surface, which indicates other surfaces will form. Charge defects studied in $SrSnO_3$ show further instability of the *A*O (due to charged Sr surface vacancies), more so than the BO_2 surface (less susceptible to Sn and O surface vacancies). With this in mind, a suitable method for manufacturing BO_2 surfaces of these materials may be to first form an *A*O surface, then treat the newly formed surface to obtain BO_2 surfaces, which supports the methodology outlined in Ref. [93]. Our main conclusion is that, although the *A*O surface is more energetically favorable, the formation of *A*-site vacancies will lead to the BO_2 surface being more prevalent than initially expected. We believe that these results will aid in future manufacturing and modeling of perovskite surfaces and also expand understanding of real long-term surface stability of these systems.

ACKNOWLEDGMENTS

The authors thank the Leverhulme for funding this research via Grant No. RPG-2021-086. The work provided by N.T.T. was supported in part by the Government Office for Science and the Royal Academy of Engineering under the UK Intelligence Community Postdoctoral Research Fellowships scheme (Grant No. ICRF2425-8-148). Via our membership of the UK's HEC Materials Chemistry Consortium, which is funded by EPSRC (Grant No. EP/R029431), this work used the ARCHER2 UK National Supercomputing Service [94]. The authors would like to acknowledge the use of the University of Exeter High-Performance Computing (HPC) facility in carrying out this work. Data retrieved from the Materials Project for $CaTiO_3$ (mp-4019), $SrTiO_3$ (mp-5229), $BaTiO_3$ (mp-5986), $CaZrO_3$ (mp-4571), $SrZrO_3$ (mp-4387), $BaZrO_3$ (mp-3834), $CaSnO_3$ (mp-4438), $SrSnO_3$ (mp-2879), and $BaSnO_3$ (mp-3163) from database version v2022.10.28 [66,67].

We acknowledge the following individuals for their contributions. N.T.T. contributed conceptualization, validation, formal analysis, investigation, data curation, writing (original draft, writing), review and editing, visualization, supervision, project administration, and funding acquisition. M.T.M. contributed validation, formal analysis, investigation, data curation, writing (original draft, writing), review and editing, and visualization. S.P.H. contributed conceptualization, formal analysis, writing (review and editing), supervision, project administration, and funding acquisition.

DATA AVAILABILITY

The data that support the findings of this study are openly available from the University of Exeter's Institutional repository [95].

[1] J. C. Gonzalez-Rosillo, S. Catalano, I. Maggio-Aprile, M. Gibert, X. Obradors, A. Palau, and T. Puig, Nanoscale correlations between metal–insulator transition and resistive switching effect in metallic perovskite oxides, Small **16**, 2001307 (2020).

[2] K. Yang, S. Nazir, M. Behtash, and J. Cheng, High-throughput design of two-dimensional electron gas systems based on polar/nonpolar perovskite oxide heterostructures, Sci. Rep. **6**, 34667 (2016).

[3] K. Eom, H. Paik, J. Seo, N. Campbell, E. Y. Tsymbal, S. H. Oh, M. S. Rzchowski, D. G. Schlom, and C.-B. Eom, Oxide two-dimensional electron gas with high mobility at room-temperature, Adv. Sci. **9**, 2105652 (2022).

[4] S. Mahatara, R. Comes, and B. Kiefer, Enhanced carrier densities in two-dimensional electron gas formed at $BaSnO_3/SrTaO_3$ and $SrSnO_3/SrTaO_3$ interfaces, J. Phys.: Condens. Matter **36**, 145001 (2024).

[5] J. Zhu, H. Li, L. Zhong, P. Xiao, X. Xu, X. Yang, Z. Zhao, and J. Li, Perovskite oxides: Preparation, characterizations, and applications in heterogeneous catalysis, ACS Catal. **4**, 2917 (2014).

[6] M. Zhang, G. Jeerh, P. Zou, R. Lan, M. Wang, H. Wang, and S. Tao, Recent development of perovskite oxide-based electrocatalysts and their applications in low to intermediate temperature electrochemical devices, Mater. Today **49**, 351 (2021).

[7] N. T. Taylor, C. J. Price, A. Petkov, M. I. Romanis Carr, J. C. Hale, and S. P. Hepplestone, The potential of overlayers on tin-based perovskites for water splitting, J. Phys. Chem. Lett. **11**, 4124 (2020).

[8] M. Kubicek, A. H. Bork, and J. L. M. Rupp, Perovskite oxides – a review on a versatile material class for solar-to-fuel conversion processes, J. Mater. Chem. A **5**, 11983 (2017).

[9] H. He, Z. Yang, Y. Xu, A. T. Smith, G. Yang, and L. Sun, Perovskite oxides as transparent semiconductors: a review, Nano Converg. **7**, 32 (2020).

[10] A. Žužić, A. Ressler, and J. Macan, Perovskite oxides as active materials in novel alternatives to well-known technologies: A review, Ceram. Int. **48**, 27240 (2022).

[11] D. Yoon, Y. Lee, Y. Kang, and J. Son, Perovskite stannate heterojunctions for self-powered ultraviolet photodiodes operated in extreme environments, Adv. Electron. Mater. **10**, 2300530 (2024).

[12] K. Tkacz-Śmiech, A. Koleżyński, and W. S. Ptak, Chemical bond in ferroelectric perovskites, Ferroelectrics **237**, 57 (2000).

[13] S. Woo, H. Jeong, S. A. Lee, H. Seo, M. Lacotte, A. David, H. Y. Kim, W. Prellier, Y. Kim, and W. S. Choi, Surface properties of atomically flat poly-crystalline $SrTiO_3$, Sci. Rep. **5**, 8822 (2015).

[14] M. Setvin, M. Reticcioli, F. Poelzleitner, J. Hulva, M. Schmid, L. A. Boatner, C. Franchini, and U. Diebold, Polarity compensation mechanisms on the perovskite surface $KTaO_3$ (001), Science **359**, 572 (2018).

[15] I. Sokolović, G. Franceschi, Z. Wang, J. Xu, J. Pavelec, M. Riva, M. Schmid, U. Diebold, and M. Setvín, Quest for a pristine unreconstructed $SrTiO_3$(001) surface: An atomically resolved study via noncontact atomic force microscopy, Phys. Rev. B **103**, L241406 (2021).

[16] F. Sánchez, C. Ocal, and J. Fontcuberta, Tailored surfaces of perovskite oxide substrates for conducted growth of thin films, Chem. Soc. Rev. **43**, 2272 (2014).

[17] Y. Wang, J. Cheng, M. Behtash, W. Tang, J. Luo, and K. Yang, First-principles studies of polar perovskite $KTaO_3$ surfaces: structural reconstruction, charge compensation, and stability diagram, Phys. Chem. Chem. Phys. **20**, 18515 (2018).

[18] B. Koo, K. Kim, J. K. Kim, H. Kwon, J. W. Han, and W. Jung, Sr segregation in perovskite oxides: Why it happens and how it exists, Joule **2**, 1476 (2018).

[19] R. Bachelet, F. Sánchez, F. J. Palomares, C. Ocal, and J. Fontcuberta, Atomically flat SrO-terminated $SrTiO_3$(001) substrate, Appl. Phys. Lett. **95**, 141915 (2009).

[20] J. Druce, H. Téllez, M. Burriel, M. D. Sharp, L. J. Fawcett, S. N. Cook, D. S. McPhail, T. Ishihara, H. H. Brongersma, and J. A. Kilner, Surface termination and subsurface restructuring of perovskite-based solid oxide electrode materials, Energy Environ. Sci. **7**, 3593 (2014).

[21] D. S. Deak, F. Silly, D. T. Newell, and M. R. Castell, Ordering of TiO_2-based nanostructures on $SrTiO_3$(001) surfaces, J. Phys. Chem. B **110**, 9246 (2006).

[22] Y. Mochizuki, H.-J. Sung, T. Gake, and F. Oba, Chemical trends of surface reconstruction and band positions of nonmetallic perovskite oxides from first principles, Chem. Mater. **35**, 2047 (2023).

[23] R. I. Eglitis and A. I. Popov, Systematic trends in (001) surface *Ab Initio* calculations of ABO_3 perovskites, J. Saudi Chem. Soc. **22**, 459 (2018).

[24] J. Li, M. Zhu, R. Feng, Y. Yuan, Z. Fu, L. Meng, Y. Wang, Y. Zhou, H. Zhang, and H. Bai, Stability and electronic properties of low-index surfaces of zinc stannate modulated by vacancy defect: A first-principle study, Physica B **659**, 414864 (2023).

[25] E. Heifets, J. Ho, and B. Merinov, Density functional simulation of the $BaZrO_3$ (011) surface structure, Phys. Rev. B **75**, 155431 (2007).

[26] X. Guo, Low temperature degradation mechanism of tetragonal zirconia ceramics in water: role of oxygen vacancies, Solid State Ion **112**, 113 (1998).

[27] K. J. May, C. E. Carlton, K. A. Stoerzinger, M. Risch, J. Suntivich, Y.-L. Lee, A. Grimaud, and Y. Shao-Horn, Influence of oxygen evolution during water oxidation on the surface of perovskite oxide catalysts, J. Phys. Chem. Lett. **3**, 3264 (2012).

[28] B. Han, K. A. Stoerzinger, V. Tileli, A. D. Gamalski, E. A. Stach, and Y. Shao-Horn, Nanoscale structural oscillations in perovskite oxides induced by oxygen evolution, Nat. Mater. **16**, 121 (2017).

[29] E. Fabbri, M. Nachtegaal, T. Binninger, X. Cheng, B.-J. Kim, J. Durst, F. Bozza, T. Graule, R. Schäublin, L. Wiles, M. Pertoso, N. Danilovic, K. E. Ayers, and T. J. Schmidt, Dynamic surface self-reconstruction is the key of highly active perovskite nano-electrocatalysts for water splitting, Nat. Mater. **16**, 925 (2017).

[30] L. Cheng, X. Yu, J. Zhang, W. Li, C. Zhao, Z. Wang, and L. Jin, DFT investigations into surface stability and morphology of δ-MoC catalyst, Appl. Surf. Sci. **497**, 143790 (2019).

[31] P. P. Lopes, D. Y. Chung, X. Rui, H. Zheng, H. He, P. F. B. D. Martins, D. Strmcnik, V. R. Stamenkovic, P. Zapol, J. F. Mitchell, R. F. Klie, and N. M. Markovic, Dynamically stable active sites from surface evolution of perovskite materials during the oxygen evolution reaction, J. Am. Chem. Soc. **143**, 2741 (2021).

[32] R. Schmidt, S. Pandey, P. Fiorenza, and D. C. Sinclair, Non-stoichiometry in "$CaCu_3Ti_4O_{12}$" (CCTO) ceramics, RSC Adv. **3**, 14580 (2013).

[33] Y. Shin, W. H. Kan, M. Aykol, J. K. Papp, B. D. McCloskey, G. Chen, and K. A. Persson, Alleviating oxygen evolution from Li-excess oxide materials through theory-guided surface protection, Nat. Commun. **9**, 4597 (2018).

[34] H. J. Heelweg and R. A. de Souza, Metadynamics simulations of strontium-vacancy diffusion in $SrTiO_3$, Phys. Rev. Mater. **5**, 013804 (2021).

[35] G. Duan, X. Li, Y. Xu, Y. Zhang, Y. Jiang, C. Hao, C. Liu, Q. Fang, J.-L. Chen, G.-N. Luo, and Z. Wang, Clustering and segregation of small vacancy clusters near tungsten (001) surface, Nucl. Instrum. Methods, Phys. Res. B **414**, 29 (2018).

[36] L. Yang, Z. J. Bergstrom, and B. D. Wirth, First-principles study of stability of helium-vacancy complexes below tungsten surfaces, J. Appl. Phys. **123**, 205108 (2018).

[37] R. Mehmood, S. S. Mofarah, W.-F. Chen, P. Koshy, and C. C. Sorrell, Surface, subsurface, and bulk oxygen vacancies quantified by decoupling and deconvolution of the defect structure of redox-active nanoceria, Inorg. Chem. **58**, 6016 (2019).

[38] N. Erdman, O. Warschkow, M. Asta, K. R. Poeppelmeier, D. E. Ellis, and L. D. Marks, Surface structures of $SrTiO_3$ (001): A TiO_2-rich reconstruction with a c(4×2) unit cell, J. Am. Chem. Soc. **125**, 10050 (2003).

[39] M. Riva, M. Kubicek, X. Hao, G. Franceschi, S. Gerhold, M. Schmid, H. Hutter, J. Fleig, C. Franchini, B. Yildiz, and U. Diebold, Influence of surface atomic structure demonstrated on oxygen incorporation mechanism at a model perovskite oxide, Nat. Commun. **9**, 3710 (2018).

[40] C. Yue, P. Ying, B. Xu, and Y. Tian, Surface reconstructions of $SrTiO_3$ (110) calibrated with STM and LEED, Phys. Status Solidi B **256**, 1900277 (2019).

[41] C. J. Pickard and R. J. Needs, *Ab initio* random structure searching, J. Phys.: Condens. Matter **23**, 053201 (2011).

[42] L. H. E. Kempen and M. Andersen, Inverse catalysts: tuning the composition and structure of oxide clusters through the metal support, npj Comput. Mater. **11**, 8 (2025).

[43] C. J. Pickard, Beyond theory-driven discovery: introducing hot random search and datum-derived structures, Faraday Discuss. **256**, 61 (2025).

[44] A. Ohtake, Surface reconstructions on GaAs(001), Surf. Sci. Rep. **63**, 295 (2008).

[45] C.-K. Sin, J. Zhang, K. Tse, and J. Zhu, A brief review of formation energies calculation of surfaces and edges in semiconductors, J. Semicond. **41**, 061101 (2020).

[46] M.-P. V. Christiansen, N. Rønne, and B. Hammer, Atomistic global optimization X: A Python package for optimization of atomistic structures, J. Chem. Phys. **157**, 054701 (2022).

[47] I. Batatia, P. Benner, Y. Chiang, A. M. Elena, D. P. Kovács, J. Riebesell, X. R. Advincula, M. Asta, M. Avaylon, W. J. Baldwin, F. Berger, N. Bernstein, A. Bhowmik, S. M. Blau, V. Cărare, J. P. Darby, S. De, F. Della Pia, V. L. Deringer, R. Elijošius *et al.*, A foundation model for atomistic materials chemistry, arXiv:2401.00096.

[48] B. Deng, P. Zhong, K. Jun, J. Riebesell, K. Han, C. J. Bartel, and G. Ceder, Chgnet as a pretrained universal neural network potential for charge-informed atomistic modelling, Nat. Mach. Intell. **5**, 1031 (2023).

[49] J. Pitfield, F. Brix, Z. Tang, A. M. Slavensky, N. Ronne, M.-P. V. Christiansen, and B. Hammer, Augmentation of universal potentials for broad applications, Phys. Rev. Lett. **134**, 056201 (2025).

[50] G. Kresse and J. Furthmüller, Efficient iterative schemes for *ab initio* total-energy calculations using a plane-wave basis set, Phys. Rev. B **54**, 11169 (1996).

[51] G. Kresse and J. Furthmüller, Efficiency of *ab-initio* total energy calculations for metals and semiconductors using a plane-wave basis set, Comput. Mater. Sci. **6**, 15 (1996).

[52] J. P. Perdew, K. Burke, and M. Ernzerhof, Generalized gradient approximation made simple, Phys. Rev. Lett. **77**, 3865 (1996).

[53] R. Armiento, B. Kozinsky, M. Fornari, and G. Ceder, Screening for high-performance piezoelectrics using high-throughput density functional theory, Phys. Rev. B **84**, 014103 (2011).

[54] M. M. Kuklja, Y. A. Mastrikov, S. N. Rashkeev, and E. A. Kotomin, The structural disorder and lattice stability of (Ba, Sr)(Co, Fe)O_3 complex perovskites, ECS Trans. **35**, 2077 (2011).

[55] R. Jacobs, J. Hwang, Y. Shao-Horn, and D. Morgan, Assessing correlations of perovskite catalytic performance with electronic structure descriptors, Chem. Mater. **31**, 785 (2019).

[56] S. A. Dar, M. A. Ali, and V. Srivastava, Investigation on bismuth-based oxide perovskites $MBiO_3$ (M = Rb, Cs, Tl) for structural, electronic, mechanical and thermal properties, Eur. Phys. J. B **93**, 102 (2020).

[57] Y. Xiong, W. Chen, W. Guo, H. Wei, and I. Dabo, Data-driven analysis of the electronic-structure factors controlling the work functions of perovskite oxides, Phys. Chem. Chem. **23**, 6880 (2021).

[58] P. Stoch, J. Szczerba, J. Lis, D. Madej, and Z. Pędzich, Crystal structure and *ab initio* calculations of $CaZrO_3$, J. Eur. Ceram. Soc. **32**, 665 (2012).

[59] N. Kuganathan, F. Baiutti, A. Morata, A. Tarancon, and A. Chroneos, Interstitial lithium doping in $SrTiO_3$, AIP Adv. **11**, 075029 (2021).

[60] M. T. Curnan and J. R. Kitchin, Effects of concentration, crystal structure, magnetism, and electronic structure method on first-principles oxygen vacancy formation energy trends in perovskites, J. Phys. Chem. C **118**, 28776 (2014).

[61] B. Medasani, M. Haranczyk, A. Canning, and M. Asta, Vacancy formation energies in metals: A comparison of MetaGGA with LDA and GGA exchange–correlation functionals, Comput. Mater. Sci. **101**, 96 (2015).

[62] E. Heifets, R. I. Eglitis, E. A. Kotomin, J. Maier, and G. Borstel, *Ab initio* modeling of surface structure for $SrTiO_3$ perovskite crystals, Phys. Rev. B **64**, 235417 (2001).

[63] A. V. Krukau, O. A. Vydrov, A. F. Izmaylov, and G. E. Scuseria, Influence of the exchange screening parameter on the performance of screened hybrid functionals, J. Chem. Phys. **125**, 224106 (2006).

[64] A. Alkauskas, P. Broqvist, and A. Pasquarello, Defect levels through hybrid density functionals: Insights and applications, Phys. Status Solidi B **248**, 775 (2011).

[65] W. Li, Z. Wang, X. Xiao, Z. Zhang, A. Janotti, S. Rajasekaran, and B. Medasani, Predicting band gaps and band-edge positions of oxide perovskites using density functional theory and machine learning, Phys. Rev. B **106**, 155156 (2022).

[66] A. Jain, S. P. Ong, G. Hautier, W. Chen, W. D. Richards, S. Dacek, S. Cholia, D. Gunter, D. Skinner, G. Ceder, and K. A. Persson, Commentary: The materials project: A materials genome approach to accelerating materials innovation, APL Mater. **1**, 011002 (2013).

[67] The Materials Project, Materials data on $CaTiO_3$, $SrTiO_3$, $BaTiO_3$, $CaZrO_3$, $SrZrO_3$, $BaZrO_3$, $CaSnO_3$, $SrSnO_3$, and $BaSnO_3$ by materials project (2020), DOIs: $CaTiO_3$: 10.17188/1207766, $SrTiO_3$: 10.17188/1263154, $BaTiO_3$: 10.17188/1272706, $CaZrO_3$: 10.17188/1208258, $SrZrO_3$: 10.17188/1208119, $BaZrO_3$: 10.17188/1207509, $CaSnO_3$: 10.17188/1208154, $SrSnO_3$: 10.17188/1202844, $BaSnO_3$: 10.17188/1205802.

[68] H. J. Monkhorst and J. D. Pack, Special points for Brillouin-zone integrations, Phys. Rev. B **13**, 5188 (1976).

[69] See Supplemental Material at http://link.aps.org/supplemental/10.1103/w683-tvc4 for further details and discussions. The topics covered include ionization energies, Gibbs free energies, comparison of formation energies calculated using DFT and machine-learned potentials, structural and electronic properties of bulk, surface formation energies and the effects of different chemical environments, vacancy formation energies, angular distortions brought on by vacancy inclusion, and energetics of native charged defects, which also includes Refs. [96–110].

[70] N. T. Taylor, F. H. Davies, I. E. M. Rudkin, C. J. Price, T. H. Chan, and S. P. Hepplestone, ARTEMIS: *Ab initio* restructuring tool enabling the modelling of interface structures, Comput. Phys. Commun. **257**, 107515 (2020).

[71] S. R. Kavanagh, A. G. Squires, A. Nicolson, I. Mosquera-Lois, A. M. Ganose, B. Zhu, K. Brlec, A. Walsh, and D. O. Scanlon,

doped: Python toolkit for robust and repeatable charged defect supercell calculations, J. Open Source Soft. **9**, 6433 (2024).

[72] Y. Kumagai and F. Oba, Electrostatics-based finite-size corrections for first-principles point defect calculations, Phys. Rev. B **89**, 195205 (2014).

[73] A. M. Z. Tan, Framework for first-principles calculations of charged dopants and defects in 2D materials, https://github.com/aztan2/charged-defects-framework.

[74] C. Freysoldt, J. Neugebauer, and C. G. Van de Walle, Fully *Ab Initio* finite-sze corrections for charged-defect supercell calculations, Phys. Rev. Lett. **102**, 016402 (2009).

[75] C. Freysoldt and J. Neugebauer, First-principles calculations for charged defects at surfaces, interfaces, and two-dimensional materials in the presence of electric fields, Phys. Rev. B **97**, 205425 (2018).

[76] A. Zaccone, Explaining the thickness-dependent dielectric permittivity of thin films, Phys. Rev. B **109**, 115435 (2024).

[77] C. Freysoldt, J. Neugebauer, A. M. Z. Tan, and R. G. Hennig, Limitations of empirical supercell extrapolation for calculations of point defects in bulk, at surfaces, and in two-dimensional materials, Phys. Rev. B **105**, 014103 (2022).

[78] D. Broberg, K. Bystrom, S. Srivastava, D. Dahliah, B. A. D. Williamson, L. Weston, D. O. Scanlon, G.-M. Rignanese, S. Dwaraknath, J. Varley, K. A. Persson, M. Asta, and G. Hautier, High-throughput calculations of charged point defect properties with semi-local density functional theory—performance benchmarks for materials screening applications, npj Comput. Mater. **9**, 72 (2023).

[79] U. Diebold, S.-C. Li, and M. Schmid, Oxide surface science, Annu. Rev. Phys. Chem. **61**, 129 (2010).

[80] S. P. Pujari, L. Scheres, A. T. M. Marcelis, and H. Zuilhof, Covalent surface modification of oxide surfaces, Angew. Chem. Int. Ed. **53**, 6322 (2014).

[81] K. Momma and F. Izumi, *VESTA 3* for three-dimensional visualization of crystal, volumetric and morphology data, J. Appl. Cryst. **44**, 1272 (2011).

[82] K. D. Fredrickson, A. B. Posadas, A. A. Demkov, C. Dubourdieu, and J. Bruley, Wetting at the $BaTiO_3$/Pt interface, J. Appl. Phys. **113**, 184102 (2013).

[83] M. Choi, F. Oba, and I. Tanaka, Electronic and structural properties of the oxygen vacancy in $BaTiO_3$, Appl. Phys. Lett. **98**, 172901 (2011).

[84] J. J. Brown, Z. Ke, W. Geng, and A. J. Page, Oxygen vacancy defect migration in titanate perovskite surfaces: Effect of the A-site cations, J. Phys. Chem. C **122**, 14590 (2018).

[85] C. Xia, Y. Chen, and H. Chen, Coexistence of polar displacements and conduction in doped ferroelectrics: An *ab initio* comparative study, Phys. Rev. Mater. **3**, 054405 (2019).

[86] L. Weston, L. Bjaalie, K. Krishnaswamy, and C. G. Van de Walle, Origins of *n*-type doping difficulties in perovskite stannates, Phys. Rev. B **97**, 054112 (2018).

[87] L. Lin, Q. Chen, Q. Zhang, J. He, H. Ni, J. Su, and C.-K. Duan, Trace impurity matters: Origin and modulation of near-infrared luminescence in stannates, Chem. Mater. **36**, 10895 (2024).

[88] J. Willis, K. B. Spooner, and D. O. Scanlon, On the possibility of p-type doping in barium stannate, Appl. Phys. Lett. **123**, 162103 (2023).

[89] Y. Zhu, W. Zheng, Y. Pan, Y. Pan, T. Liu, X. Zhou, D. Shi, Y. Shi, and X. Wei, Formation and binding energies of vacancies in the Al(111) surface: Density functional theory calculations confirm simple bond model, Surf. Sci. **637-638**, 85 (2015).

[90] M. Behtash, Y. Wang, J. Luo, and K. Yang, Oxygen vacancy formation in the $SrTiO_3\sigma 5$ [001] twist grain boundary from first-principles, J. Am. Ceram. Soc **101**, 3118 (2018).

[91] R. He, J. L. Lin, Q. Liu, Z. Liao, L. Shui, Z. J. Wang, Z. Zhong, and R.-W. Li, Emergent ferroelectricity in otherwise nonferroelectric oxides by oxygen vacancy design at heterointerfaces, ACS Appl. Mater. Interfaces **12**, 45602 (2020).

[92] G. R. Monama, K. E. Ramohlola, E. I. Iwuoha, and K. D. Modibane, Progress on perovskite materials for energy application, Results Chem. **4**, 100321 (2022).

[93] M. Kawasaki, K. Takahashi, T. Maeda, R. Tsuchiya, M. Shinohara, O. Ishiyama, T. Yonezawa, M. Yoshimoto, and H. Koinuma, Atomic control of the $SrTiO_3$ crystal surface, Science **266**, 1540 (1994).

[94] http://www.archer2.ac.uk.

[95] N. T. Taylor, M. Morgan, and S. P. Hepplestone, Instability of ABO_3 perovskite surfaces induced by vacancy formation (A = Ca, Sr, Ba; B = Ti, Zr, Sn) - Dataset, Figshare repository, https://doi.org/10.6084/m9.figshare.28844996.

[96] *CRC Handbook of Chemistry and Physics*, edited by W. M. Haynes, D. R. Lide, and T. J. Bruno (CRC Press, Boca Raton, FL, 2016).

[97] Z.-J. Suo, J.-W. Luo, S.-S. Li, and L.-W. Wang, Image charge interaction correction in charged-defect calculations, Phys. Rev. B **102**, 174110 (2020).

[98] R. B. Wexler, G. S. Gautam, E. B. Stechel, and E. A. Carter, Factors governing oxygen vacancy formation in oxide perovskites, J. Am. Chem. Soc. **143**, 13212 (2021).

[99] N. T. Taylor, J. Pitfield, F. H. Davies, and S. P. Hepplestone, RAFFLE: Active learning accelerated interface structure prediction, arXiv:2504.02528.

[100] S. Kim, S. N. Hood, J.-S. Park, L. D. Whalley, and A. Walsh, Quick-start guide for first-principles modelling of point defects in crystalline materials, Acad. J. Phys. Energy **2**, 036001 (2020).

[101] G. Fischer, Z. Wang, and S. ichiro Karato, Elasticity of $CaTiO_3$, $SrTiO_3$ and $BaTiO_3$ perovskites up to 3.0 GPa: the effect of crystallographic structure, Phys. Chem. **20**, 97 (1993).

[102] I. Levin, T. G. Amos, S. M. Bell, L. Farber, T. A. Vanderah, R. S. Roth, and B. H. Toby, Phase equilibria, crystal structures, and dielectric anomaly in the $BaZrO_3$–$CaZrO_3$ system, J. Solid State Chem. **175**, 170 (2003).

[103] L. M. C. Honorio, M. V. B. Santos, E. C. da Silva Filho, J. A. Osajima, A. S. Maia, and I. M. G. dos Santos, Alkaline earth stannates applied in photocatalysis: prospection and review of literature, Cerâmica **64**, 559 (2018).

[104] C. Yuan, S. Ye, B. Xu, and W. Lei, Strain induced tetragonal $SrTiO_3$ nanoparticles at room temperature, Appl. Phys. Lett. **101**, 071909 (2012).

[105] R. I. Eglitis, *Ab initio* calculations of $SrTiO_3$, $BaTiO_3$, $PbTiO_3$, $CaTiO_3$ and $BaZrO_3$ (001) and (011) surfaces, Integr. Ferroelectr. **108**, 11 (2009).

[106] R. I. Eglitis, *Ab initio* calculations of $CaZrO_3$, $BaZrO_3$, $PbTiO_3$ and $SrTiO_3$ (001), (011) and (111) surfaces as well as their (001) interfaces, Integr. Ferroelectr. **196**, 7 (2019).

[107] A. Slassi, M. Hammi, and O. E. Rhazouani, Surface relaxations, surface energies and electronic structures of $BaSnO_3$

(001) surfaces: *Ab Initio* calculations, J. Electron. Mater. **46**, 4133 (2017).

[108] X. Zhao and A. Selloni, Structure and stability of $NaTiO_3$(001) and $KTaO_3$(001) surfaces, Phys. Rev. Mater. **3**, 015801 (2019).

[109] R. I. Eglitis and D. Vanderbilt, *Ab initio* calculations of $BaTiO_3$ and $PbTiO_3$ (001) and (011) surface terminations, Phys. Rev. B **76**, 155439 (2007).

[110] K. Lejaeghere, G. Bihlmayer, T. Björkman, P. Blaha, S. Blügel, V. Blum, D. Caliste, I. E. Castelli, S. J. Clark, A. Dal Corso, S. de Gironcoli, T. Deutsch, J. K. Dewhurst, I. Di Marco, C. Draxl, M. Dułak, O. Eriksson, J. A. Flores-Livas, K. F. Garrity, L. Genovese *et al.*, Reproducibility in density functional theory calculations of solids, Science **351**, aad3000 (2016).